ARTICLE

Multimodality of Structural, Electrical, and Gravimetric Responses of Intercalated MXenes to Water

Eric S. Muckley,[†,¶,○] Michael Naguib,*[,‡,○] Hsiu-Wen Wang,[§] Lukas Vlcek,[§] Naresh C. Osti,[⊥] Robert L. Sacci,[‡] Xiahan Sang,[†] Raymond R. Unocic,[†] Yu Xie,[†] Madhusudan Tyagi,[#,△] Eugene Mamontov,[⊥] Katharine L. Page,[⊥] Paul R. C. Kent,[†,‖] Jagjit Nanda,[‡,¶] and Ilia N. Ivanov*[,†,¶]

[†]Center for Nanophase Materials Sciences, [‡]Materials Science and Technology Division, [§]Chemical Sciences Division, [⊥]Chemical and Engineering Materials Division, and [‖]Computer Science and Mathematics Division, Oak Ridge National Laboratory, Oak Ridge, Tennessee 37831, United States

[¶]Bredesen Center for Energy Science and Engineering, University of Tennessee, Knoxville, Tennessee 37996, United States

[#]NIST Center for Neutron Research, National Institute of Standards and Technology, 100 Bureau Drive, MS 6100, Gaithersburg, Maryland 20899, United States

[△]Department of Materials Science, University of Maryland, 4418 Stadium Drive, College Park, Maryland 20740, United States

Ⓢ *Supporting Information*

ABSTRACT: Understanding of structural, electrical, and gravimetric peculiarities of water vapor interaction with ion-intercalated MXenes led to design of a multimodal humidity sensor. Neutron scattering coupled to molecular dynamics and *ab initio* calculations showed that a small amount of hydration results in a significant increase in the spacing between MXene layers in the presence of K and Mg intercalants between the layers. Films of K- and Mg-intercalated MXenes exhibited relative humidity (RH) detection thresholds of ~0.8% RH and showed monotonic RH response in the 0−85% RH range. We found that MXene gravimetric response to water is 10 times faster than their electrical response, suggesting that H_2O-induced swelling/contraction of channels between MXene sheets results in trapping of H_2O molecules that act as charge-depleting dopants. The results demonstrate the use of MXenes as humidity sensors and infer potential impact of water on structural and electrical performance of MXene-based devices.

KEYWORDS: *MXene, intercalation, pillaring, neutron scattering, quartz crystal microbalance, humidity sensor*
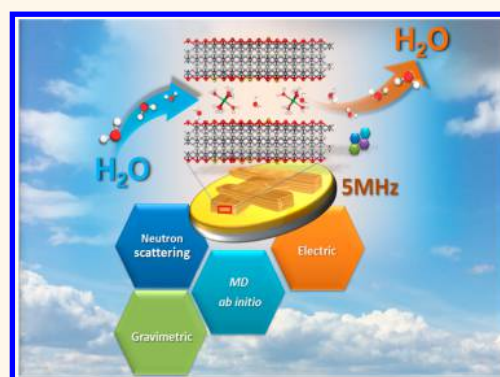
MXenes are large family of two-dimensional (2D) materials of transition metal carbides and carbonitrides.[1−3] MXenes are produced by etching A layers from MAX ($M_{n+1}AX_n$) phases,[2,3] where M is an early transition metal, A is a group IIIA or IVA element, and X is carbon or nitrogen with n = 1, 2, or 3.[4] Of over a dozen different MXenes synthesized to date, the most widely investigated MXene is Ti_3C_2,[2] which has garnered attention for its exceptional performance in supercapacitors, batteries, water purification, composites for flexible electronics, and sensors.[1,5−10]

MXenes are electrically conductive and capable of hosting a wide variety of ionic[1,7] and molecular species in their galleries.[11] MXenes surfaces are terminated by O, OH, and F making them hydrophilic.[12,13] Of particular interest is H_2O sorption/intercalation, which could lead to significant structural and electrochemical changes in properties of MXene films.[7,14]

Understanding the H_2O−MXene interaction is complicated by saturation of MXene flakes by hydrophilic surface groups[15] and coordination of H_2O to intercalated cations.[7] The presence of cations intercalated between individual MXene sheets influences H_2O diffusion during hydration/dehydration processes[14] and affects H_2O-induced swelling in multilayered MXene sheets.[7] However, it is still unclear if interaction with H_2O affects the chemical composition of MXenes. In TiC, even the least reactive crystal face reacts with adsorbed H_2O, leading to formation of TiO_2, CO, CO_2, and H_2.[16,17]

While effects of H_2O sorption on the *c*-lattice parameters of MXenes have been studied,[7,14] the electronic effects originating

from H_2O exposure are less understood, especially in the presence of intercalated ions. Adsorption of oxygen on titanium carbide surfaces can lead to O_2 dissociation due to charge transfer between O and Ti,[12,15] so one would expect that dissociative interaction of MXene surfaces with H_2O may also lead to complex charge transfer effects.

Despite their hydrophilic nature and tunable electrical properties, MXenes have not been explored for gas or humidity sensing applications. This could be due to their high conductivity,[1] which may limit electrical response to gas/vapor adsorption. The ability of ion-intercalated MXenes to take up H_2O between stacks of multilayers and individual exfoliated layers[14] makes MXenes attractive candidates for relative humidity (RH) sensing. Understanding the hydration/dehydration and corresponding electrical response of MXenes is crucial for the design of MXene-based electronics and environmental sensors.

Here, we report on the change in MXene structure upon hydration using neutron scattering and resistive H_2O response of Ti_3C_2 MXenes intercalated with K and Mg cations. We correlate the resistive response to gravimetric-based RH sensing using a quartz crystal microbalance (QCM) with sub-0.1 Hz resolution. We also estimated the amount of intercalated water between MXene sheets. Understanding MXene−water interaction is important for the development of MXene-enabled architectures and technologies, including high-performance aqueous super-capacitors.[8,9] Neutron scattering was used to determine hydrogen content of dry MXenes, and classical molecular dynamics coupled with *ab initio* calculations were used to explain the experimental results.

RESULTS AND DISCUSSION

The *c*-lattice parameters of the synthesized K^+- and Mg^{2+}-intercalated titanium carbide MXene (referred to as Ti_3C_2-K and Ti_3C_2-Mg, respectively) were determined to be 24.78 and 29.24 Å, respectively, from X-ray diffraction measurements (Figure S1). The parameters agree with those reported by Ghidiu *et al.* at relative humidity >10%, and they are significantly larger than that of non-intercalated Ti_3C_2 (non-intercalated ∼19−20 Å).[7] These large *c*-lattice parameters were speculated to be a result of H_2O adsorption between layers of K- and Mg-intercalated MXenes.[7]

Due to the high neutron scattering cross section of hydrogen isotopes, neutron scattering was used to probe H_2O intercalation. In Figure 1a,b, the normalized scattering intensity with respect to vanadium rod scattering is displayed for Ti_3C_2-K and Ti_3C_2-Mg, along with scattering of non-intercalated $Ti_3C_2T_x$ (Wang *et al.*,[18] $Ti_3C_2[O_{0.1(1)},(OH)_{1.0(1)},F_{0.8(1)}]$). Because H-nucleus has a large incoherent cross section, the sample-dependent background can be used to estimate the amount of protons from terminal −OH or intercalated H_2O molecules. In Figure 1a−c, the background increases with hydration in both the low- and high-Q regions. The dry Ti_3C_2-K and Ti_3C_2-Mg showed no detectable amounts of hydrogen, suggesting the absence of terminal −OH and H_2O, as opposed to non-intercalated Ti_3C_2, which contained OH groups. This agrees with previous results that ion-assisted acid-etched MXenes contained less OH compared to those prepared with conventional HF etching.[19] The cation/H_2O-intercalated MXenes contain an insignificant amount of H_2O between layers, suggesting that the observed *d*(002) basal space can be maintained without continuous H_2O coverage (more discussions are given below). We estimated the proton content in the hydrated samples through interpolation of the neutron background intensity using
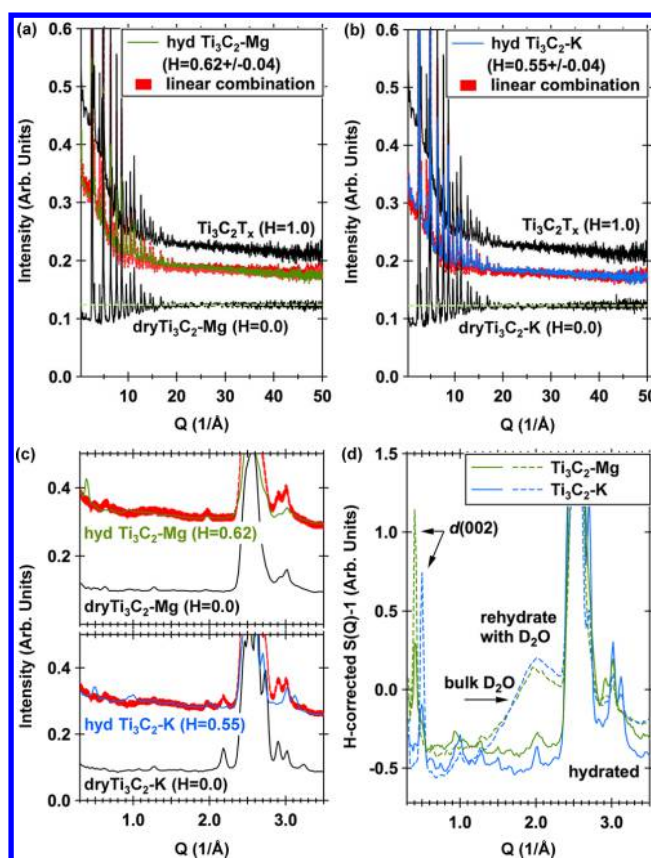

Figure 1. (a,b) Normalized neutron intensities with respect to vanadium rod scattering for hydrated and dry Mg- and K-intercalated MXenes, referenced to non-intercalated $Ti_3C_2T_x$ sample. Data for linear interpolation are shown in red, and the hydrated sample data are shown in green for Mg and blue for K. (c) Expanded view in the low-Q region of plots (a) and (b). (d) Hydrogen-corrected total scattering structure factor $S(Q)$ for hydrated and D_2O rehydrated Mg- and K-intercalated MXenes. Position of the *d*(002) peak is 15.2(2) and 12.8(2) Å for Mg- and K-intercalated MXene, respectively. Error bars throughout the text represent one standard deviation.

two samples with known H content, a non-intercalated sample with H content of 1, and a dry sample with H content of 0 per Ti_3C_2 formula. The interpolation results and H content estimation with upper and lower uncertainties are provided in Figure 1a−c (red area curve) and Table 1.

Table 1 summarizes estimated H content and sample stoichiometry based on the interpolation method, along with atomic fractions of O, F, Mg and K (with respect to the Ti_3C_2 formula unit) obtained from energy-dispersive X-ray (EDX) spectroscopy analysis. To verify the results, we recalculated scattering ratio of high- and low-Q values based on proton stoichiometry estimated by interpolation. The obtained scattering values (Table 1) agree well with those obtained by direct calculation and data interpolation. Uncertainties in H content are estimated to be in the range between 5 and 10%. Figure 1d shows the final hydrogen-corrected total scattering structure factor, $S(Q)$. Here, we compare the hydrated samples with rehydrated ones (rehydration is performed *via* immersing dry samples in bulk D_2O). The *c*-lattice parameter was recovered, which suggests that water intercalation is reversible.

We used a combination of classical molecular dynamics and density functional theory (DFT) simulations to interpret the

Table 1. Estimated H Content for the Non-intercalated, Hydrated, and Dry Ti_3C_2-Mg and Ti_3C_2-K MXenes

sample name	observed background intensity[a]		calculated scattering value		stoichiometry[b] and estimated H content
	low-Q	high-Q	low-Q	high-Q	
hyd Ti_3C_2-Mg	0.329	0.180	0.334(13)	0.179(3)	$Ti_3C_2[O_{1.26},F_{0.74}]$-$Mg_{0.07}(H_2O)_{0.31(2)}$ (H = 0.62(4))
hyd Ti_3C_2-K	0.313	0.174	0.307(13)	0.170(3)	$Ti_3C_2[O_{1.24},F_{0.76}]$-$K_{0.14}(H_2O)_{0.28(2)}$ (H = 0.55(4))
dry Ti_3C_2-Mg	0.119	0.124	0.113(10)	0.125(3)	$Ti_3C_2[O_{1.26},F_{0.74}]$-$Mg_{0.07}$ (H = 0)
dry Ti_3C_2-K	0.106	0.123	0.110(10)	0.123(3)	$Ti_3C_2[O_{1.24},F_{0.76}]$-$K_{0.14}$ (H = 0)
non-intercalated	0.474	0.216	0.479(10)	0.218(3)	$Ti_3C_2[O_{0.1},(OH)_{1.0},F_{0.8}]$ (H = 1)

[a]The hydrogen background was estimated using a pseudo-Voigt function nonlinear least-squares fitting approach. [b]Atomic fractions of O, F, Mg, and K with respective to Ti_3C_2 formula unit were reported based on energy-dispersive X-ray spectroscopy analyses.

experimental response of K⁺- and Mg²⁺-intercalated MXenes to hydration. In the case of the dry Ti_3C_2-K and Ti_3C_2-Mg, the simulation box contained 126 atoms forming two MXene layers with solely O or F termination and one K⁺ and Mg²⁺ in each of the two galleries (insets of Figure 2). For K-Ti_3C_2, the resulting
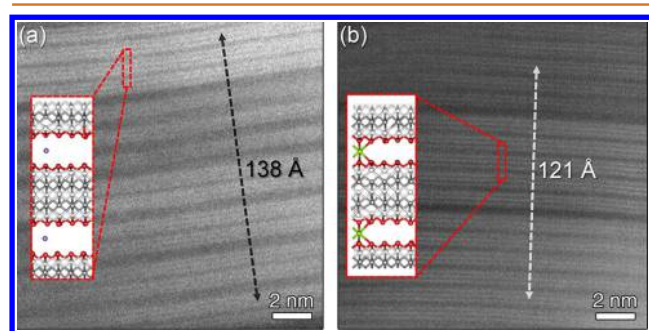

Figure 2. STEM cross-section images for (a) K⁺- and (b) Mg²⁺-intercalated MXene. The insets in (a,b) are DFT-MD simulation snapshots of K⁺- and Mg²⁺-intercalated in MXene, respectively. K (purple), Mg (greed), O (red), C (light gray), Ti (dark gray).

(002) d-spacing was found to be 10.35 and 10.50 Å with F and O terminations, respectively (the d-spacing values from both theoretical calculations and experimental values are listed in Table 2). The d-spacing was found to be 9.65 and 9.60 Å for

Table 2. Experimentally Measured and Calculated d-Spacing Values for Dry and Hydrated Ti_3C_2-K and Ti_3C_2-Mg

sample	d-spacing, Å				
	dry			hydrated	
	exptl	calcd		exptl	calcd
		O	F		O−F mixture
Ti_3C_2-K	11.5	10.50	10.35	12.4	11.2[a]
Ti_3C_2-Mg	10.1	9.60	9.65	14.6	14.3[a] (14.75)[b]

[a]Averaged value for 5 ps simulation time from DFT-MD calculations. [b]Total classical MD simulation time of 100 ps.

Ti_3C_2-Mg with F and O terminations, respectively. Scanning transmission electron microscopy (STEM) images for Ti_3C_2-K and Ti_3C_2-Mg are shown in Figure 2a,b. The average spacing between Ti_3C_2-K and Ti_3C_2-Mg layers was found to be 11.5 and 10.1 Å, respectively. These values are slightly larger than what was estimated by DFT, but they show that galleries of Ti_3C_2-K are larger than Ti_3C_2-Mg in the dry state. The small variation between the DFT and the STEM images can be explained by residual water between the layers. Water intercalation has been attributed to increases in the layer spacing of V_2CT_x, Nb_2CT_x,[20] and $Nb_4C_3T_x$ MXenes.[21] Ghidiu et al.[7] observed similar d-

spacing increases in Mg²⁺-, Na⁺-, Li⁺-, and Ca²⁺-intercalated MXenes during water adsorption.

Theoretical calculations have been able to predict and explain MXene behavior.[22] Here, we present results from DFT-MD simulations of the hydrated MXenes using the MXenes modeled in Figure 2, with two H_2O per K⁺ and five H_2O per Mg²⁺ ion to match the experimental H/cation ratio in Table 1. F and O terminations were added to match the experimentally determined composition (Figure 3a). The structure was allowed to relax over 5 ps.
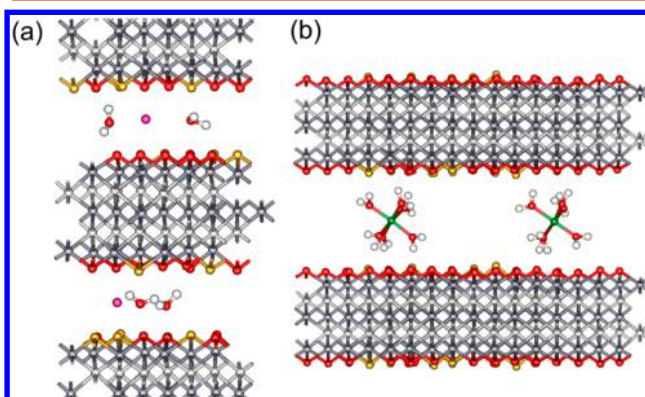

Figure 3. (a) DFT-MD simulation snapshot of K⁺ $(H_2O)_2$ in MXene pores. K (purple), O (red), F (yellow), C (light gray), Ti (dark gray). (b) DFT-MD simulation snapshot of Mg²⁺$(H_2O)_6$ clusters in MXene pores. Mg (green), O (red), F (yellow), C (light gray), Ti (dark gray).

Average d-spacing was found to be 11.2 and 15 Å in Ti_3C_2-K and Ti_3C_2-Mg, with an average of 5 H_2O molecules coupled to each Mg ion. Such a small amount of water cannot completely fill the interlayer spaces, but hydrated ions may further increase distance between MXene sheets. We tested the hypothesis that strongly bonded Mg−H_2O clusters can act as pillars between the MXene sheets. The Mg$(H_2O)_6$ cluster is the best candidate for the pillaring effect because water molecules completely fill the first hydration shell, resulting in a rigid structure.

Because the original simulation cell is too small to accommodate a fully hydrated ion without the hydration shell interacting with itself, we expanded the simulation cell laterally and placed two clusters between MXene layers to approximate the average ion concentration per surface unit. The new simulation cell contains 504 atoms and two Mg$(H_2O)_6$ clusters within the same layer. To prevent artifacts caused by interaction of a MXene sheet with itself, we included two MXene layers separated by a vacuum (Figure 3b). In this bilayer setup, the Mg$(H_2O)_6$ clusters were stable and supported the MXene sheets at a separation corresponding to d-spacing = 14.3 Å as measured between the central layer Ti atoms of each MXene sheet after 5
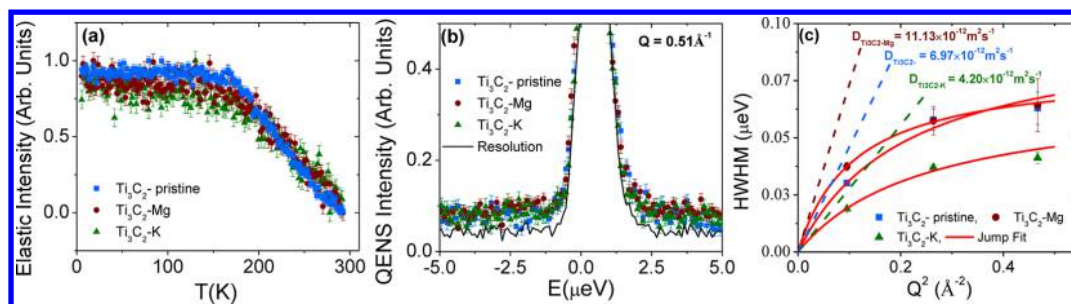
Figure 4. (a) Normalized elastic intensity from dry MXene samples measured in temperature range from 20 to 300 K at intervals of 2 K (samples were annealed at 110 °C under vacuum prior to experiments). (b) Normalized QENS spectra measured at 300 K from the same samples at a representative $Q = 0.51$ Å^{-1}. Also shown is the instrument resolution (black line) measured at 4 K. QENS spectra intensities at the elastic peak have been truncated for clarity. (c) Dependence of half-width at half-maximum extracted from the model fit on Q^2. Solids lines are jump diffusion model fits. The extracted water diffusion coefficient values are shown.

ps. The close agreement between the experimentally determined expansion of 4.5 Å and that from DFT of 4.7 Å indicates that the proposed hypothesis is correct. Formation of Mg(H$_2$O)$_6$ clusters can lead to the experimentally observed increase in lattice constants.

To confirm the (meta-)stability of the pillars, we performed classical MD simulations of the hydrated Mg^{2+} clusters over longer time spans using a simple force field with parameters defined in Tables S1−S3. Simulations were performed in a similar configuration to the DFT-MD with two clusters between two MXene layers, and results were integrated into DFT calculations. The classical MD simulations showed that hydrated Mg^{2+} clusters were stable for over 100 ps, supporting a d-spacing of 14.75 Å.

Calculated and experimentally measured d-spacing in non-hydrated Ti$_3$C$_2$-K is larger than that of Ti$_3$C$_2$-Mg due to the larger dry ionic radius of K$^+$ (1.33−1.50 Å) compared to that of Mg^{2+} (0.65−0.85 Å).[23] The smaller size and stronger charge of Mg^{2+} enables stronger coupling with H$_2$O (kosmotropic behavior), which results in a hydrated radius of Mg^{2+} (~4.28 Å) larger than that of K$^+$ (~3.31 Å).[24] Upon hydration, the larger hydrated Mg^{2+} radius leads to larger hydrated d-spacing in Ti$_3$C$_2$-Mg (Table 2).

We collected quasi-elastic neutron scattering (QENS) data on partially dehydrated pristine Ti$_3$C$_2$, Ti$_3$C$_2$-K, and Ti$_3$C$_2$-Mg to study the mobility of water confined in sub-nanometer galleries between MXene layers (Figure 4). QENS data were collected using 110 °C annealed samples. The lower annealing temperature used for QENS experiment (110 °C) was selected to remove bulk water from the samples while keeping intercalated water.[14] The onset of measurable diffusion dynamics of the confined water, in temperature dependence of elastic intensity, suggests that all samples contain a detectable amount of water, similar to a previous report on Ti$_3$C$_2$ MXene.[14] The elastic scattering intensity decreases at ~200 K, revealing that water is mobile and confined within galleries (no sign of bulk-like water in the samples) (Figure 4a). Pristine Ti$_3$C$_2$ showed the highest elastic intensity, followed by Ti$_3$C$_2$-Mg and Ti$_3$C$_2$-K MXenes. However, the QENS spectra presented in Figure 4b do not show any significant difference in quasi-elastic broadening between the pristine and K- and Mg-intercalated MXenes. This observation suggests that pristine MXene might have more immobile hydrogen bearing species, which contribute only to the elastic scattering intensity, likely −OH groups.

The measured spectra, $I(Q,E)$, at each Q value was fitted using a model function represented by

$$I(Q, E) = [p_1(Q)\delta(E) + (1 - p_1(Q))S(Q, E)]$$
$$\otimes R(Q, E) + B(Q, E) \quad (1)$$

Here, $p_1(Q)$, $\delta(E)$, and $S(Q,E)$ are elastic incoherent scattering function, a Dirac delta function, and the quasi-elastic contribution, respectively. Data were convoluted with instrument resolution and $R(Q,E)$. $B(Q,E)$ is a fitted linear background term added during the data analysis. $S(Q,E)$ was modeled to a Lorentzian peak to capture the diffusion dynamics of the confined water in MXenes as follows:

$$S(Q, E) = \frac{1}{\pi}\frac{\Gamma(Q)}{\Gamma^2(Q) + E^2} \quad (2)$$

where $\Gamma(Q)$ is the half-width at half-maximum (hwhm) of the Lorentzian peak.

Dependence of the hwhm on Q^2, as shown in Figure 4c, reflects jump diffusion behavior of water molecules in all the MXene samples studied. Diffusion coefficients (D) extracted from jump diffusion model[25] are 2 orders of magnitude smaller compared to bulk value[26] and the diffusion coefficient reported for non-intercalated MXenes synthesized using stronger etchant (48% HF).[14] After ion intercalation, water is confined between the individual MXene layers with much slower dynamics than water associated with the MXene surface.[14] Thus, the smaller diffusion coefficient reported here confirms that the majority of water resides between the MXene layers.

Water mobility in Ti$_3$C$_2$-K ($D = 4.2 \times 10^{-12}$ m^2 s^{-1}) was found to be more suppressed than that of pristine Ti$_3$C$_2$ ($D = 6.9 \times 10^{-12}$ m^2 s^{-1}), possibly due to the combined effect of the spatial confinement[27] and strong K$^+$ ion−water hydration complex. We found that water molecules in the interlayer space of Ti$_3$C$_2$-Mg ($D = 11.1 \times 10^{-12}$ m^2 s^{-1}) are more mobile. Considering that Mg^{2+} forms a stronger hydration complex compared to K$^+$, which should result in slower dynamics of water for Ti$_3$C$_2$-Mg, the contradicting results measured here indicate that the d-spacing (d-spacing of Ti$_3$C$_2$-Mg > Ti$_3$C$_2$-K) has a dominant effect compared to the nature of ion−water hydration complex. Similar observation was reported from QENS studies of hydrated clay systems.[28,29] Mobility of H$_2$O inside the MXenes suggests that the response time of a MXene humidity sensor would be on the order of 100 s. Any additional process, such as chelation or complex migration, would increase response time. It is worth noting that all the QENS measurements were conducted on samples after vacuum annealing at 110 °C. Thus, the water mobility values discussed above can be considered the lower limit as they reflect mobilities of confined water.
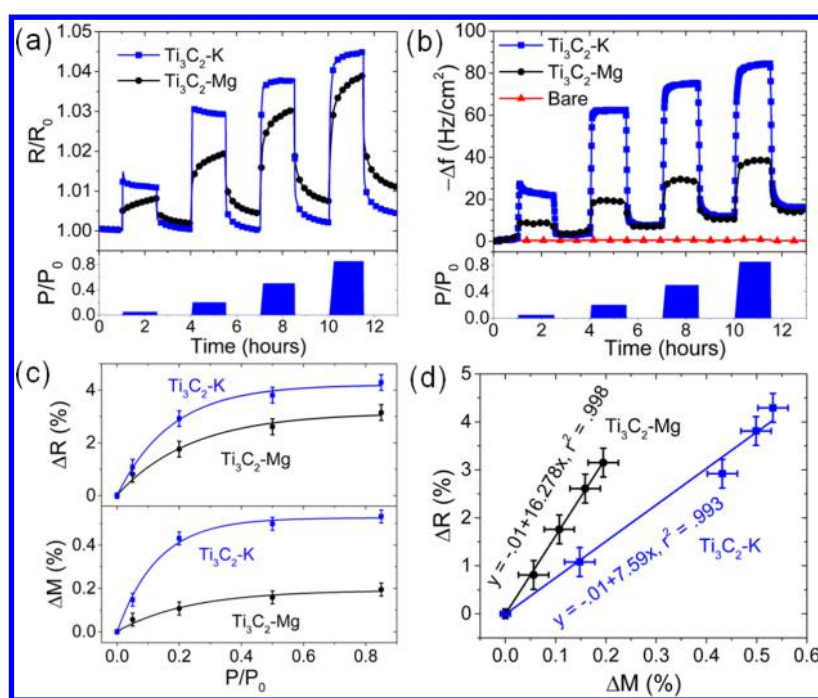
Figure 5. (a) Normalized resistance change (R/R_0) of K- and Mg-intercalated MXenes during exposure to water vapor. H_2O pressure (P/P_0) is shown in the lower panel, where P_0 is the H_2O saturation pressure at 27 °C (~23.8 Torr). (b) Normalized frequency shift (Δf) under the same RH conditions. For reference, frequency shift of a bare Au-coated crystal is shown in red. (c) Changes in ΔR and ΔM (film mass) as a function of P/P_0 are shown with corresponding exponential fits. (d) Changes in ΔR as a function of ΔM are shown with corresponding linear fits.

Water interaction with K- and Mg-intercalated MXenes may produce electrical and gravimetric responses in MXene films which can be used for water vapor sensing. Figure 5a,b shows electrical resistance (ΔR) and frequency shift (Δf) when K- and Mg-intercalated MXene films on interdigitated electrodes and QCM crystals were exposed to water vapor. The changes in ΔR can be attributed to electronic decoupling of individual MXene layers due to interlayer space increase,[7] charge depletion in the presence of adsorbed H_2O,[12,15] and H_2O-induced chemical modification of the MXene surface.[16,17] Ti_3C_2-K exhibited larger changes in resistance and frequency shift than Ti_3C_2-Mg. The results are consistent with stoichiometric analysis and water-submerged QCM experiments. EDX analysis showed that concentration of K^+ ions is roughly twice as high as concentration of Mg^{2+} ions (Table 1) resulting in ~50% more water per unit cell in Ti_3C_2-K than in Ti_3C_2-Mg (estimated using water submerged QCM as shown in Table S4). This suggests that water capacity of the hydrated MXene network depends on cation concentration rather than d-spacing, and therefore, the MXene formula should indicate the amount of intercalated ions (Ti_3C_2-$K_{0.14}$ and Ti_3C_2-$Mg_{0.07}$). The resistive response of MXenes to water vapor pulses is shown in Figure 5a. Electrical resistance of the Ti_3C_2-Mg film continued to increase during 90 min of water exposure, whereas that of Ti_3C_2-K film reached stabilization much faster (~50 min). Ti_3C_2-K films also showed higher reversibility, with >90% of the initial value of resistance and frequency shift being fully recoverable after 90 min, compared to 80−85% recovery for Ti_3C_2-Mg. We speculate that the partial irreversibility is due to trapped water between MXene layers, leading to hysteresis in the hydration/dehydration dynamics of Ti_3C_2-Mg.

Using the Sauerbrey equation[30] and frequency shift of the QCM crystals, we estimated that with a 10 s gate time the gravimetric sensor detects 0.025% change in mass of MXene film,

corresponding to ~35 ng of H_2O per ~140 μg of MXene film. The Sauerbrey equation is valid only for acoustically thin rigid films, which are tightly bound to the surface of the quartz oscillator. Changes in viscoelastic properties of the film and slipping at the film/crystal interface complicate the relationship between frequency shift and mass change.[31] Shpigel et al.[32] showed that viscoelastic contributions to frequency shift are generally non-negligible. Here, we assumed that frequency shift primarily reflects mass change in the MXene films, and we used the Sauerbrey equation to estimate mass change from Δf. Figure 5c shows a correlation between changes in electrical resistance (ΔR) and film mass (ΔM) after 90 min of H_2O vapor exposure at different partial pressures. At $P/P_0 > 0.5$, changes in ΔR and ΔM became small. This likely occurred after all interlayer spaces are saturated. Figure 5d shows the relationship between resistance and mass change during H_2O adsorption, which is nearly linear for both Ti_3C_2-K and Ti_3C_2-Mg, suggesting that H_2O sorption is responsible for observed changes. We estimated that MXene-based RH sensors achieve resolution of ~3% RH. The detection limit was estimated to be ~0.2 Torr partial pressure H_2O (corresponding to $P/P_0 = 0.8$%) for both resistive and gravimetric-based sensing. Sensitivity and detection limits were estimated from Figure 5c,d by comparing the response to the background signal. We demonstrated that K- and Mg-intercalated MXene humidity sensors can operate in ~0−85% RH range at room temperature. This is comparable to performance of RH sensors based on metal oxides, which show 2% RH sensitivity in 5−99% RH range,[33] graphene oxide sensors which show 4% RH sensitivity in 11−95% RH range,[34] and conjugated polymers which show 1% RH sensitivity in 33−97% RH range.[35,36]

Differences in Ti_3C_2-K and Ti_3C_2-Mg H_2O desorption kinetics are shown in Figure 6. The ΔR and ΔM responses were modeled using an exponential decay
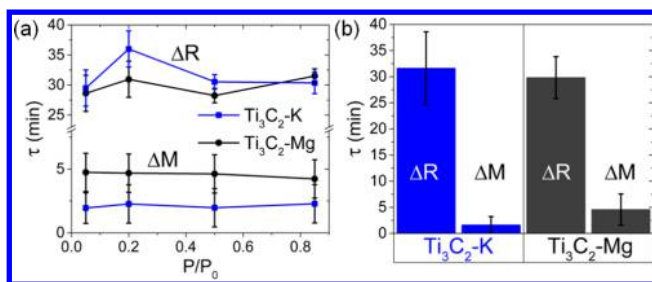
Figure 6. (a) Exponential time constant (τ) for ΔR and ΔM responses during H_2O desorption. Note the break in the y-axis. (b) Comparison of average value of τ in Ti_3C_2-K and Ti_3C_2-Mg.

$$y = y_0 e^{-t/\tau} \tag{3}$$

where τ is the time constant. As shown in Figure 6a, H_2O partial pressure did not have a significant effect on τ. The average values of τ for ΔR and ΔM responses to H_2O desorption in Ti_3C_2-K and Ti_3C_2-Mg are shown in Figure 6b. In both materials, the value of τ for the resistive response was larger than τ for the mass change by nearly an order of magnitude, suggesting that H_2O adsorption/desorption is faster than the corresponding electronic changes. Adsorption/desorption of the majority of H_2O occurred on a time scale of 5 min or less, whereas recovery of the electrical resistance occurred on a much longer time scale (~30 min).

Finally, we investigated the effect of air and temperature on the ΔR and ΔM responses of Ti_3C_2-K and Ti_3C_2-Mg. Figure S2a shows the resistance change of MXenes during exposure to 10^{-3} Torr vacuum after films were exposed to ambient air. Over a period of 10 h in vacuum, the resistance of K- and Ti_3C_2-Mg decreases by ~14 and 7%, respectively. The change in resistance upon transition of film from air to vacuum is ~5% larger than the response to transition from vacuum to 85% RH. This suggests that air has a large effect on the electrical properties of the MXenes, and the effect is semireversible upon exposure to vacuum. This suggests that MXenes may undergo charge transfer interaction with components of ambient air. Partial oxidation of MXene flake edges in the presence of air could contribute to the irreversibility.[37]

QCM proved itself to be a very powerful technique to study intercalation of 2D electrodes in electrochemical energy storage systems.[32,38] We studied behavior of MXene films submerged in water using QCM (Table S4). Ethanol was chosen as reference liquid as MXene-coated QCM submerged in ethanol showed no detectable change in frequency. The addition of water to ethanol caused a decrease in oscillation frequency (increase in mass) of K- and Mg-intercalated MXene films but not in the pristine MXene, and Ti_3C_2-K adsorbs more H_2O than Ti_3C_2-Mg per unit formula of $Ti_3C_2T_x$. These results agree with results of water vapor adsorption experiments in K- and Mg-intercalated MXene films (Figure 5). The results of thermal gravimetric analysis (Figure S2b) suggest that Ti_3C_2-Mg releases less H_2O upon dehydration than Ti_3C_2-K, which correlates with the results of water absorption on submerged MXene films. Future studies will focus on effect of cations on dynamics of water–MXene interaction.

CONCLUSIONS

K-and Mg-intercalated MXenes were investigated as active materials for resistive and gravimetric RH sensing. Neutron scattering combined with *ab initio* calculations showed that

intercalation of an average two water molecules per K^+ ion and five molecules per Mg^{2+} ion led to a pillaring effect which led to an increase in the c-lattice parameters of K- and Mg-intercalated MXenes. By exposing the MXenes to pulses of water vapor and measuring resistance and mass changes in the films, we showed that MXene-based RH sensors had detection limits of ~0.8% RH and can be used in the 0−85% RH range with ~3% resolution. The resistive response to H_2O desorption is slower than mass response by about an order of magnitude due to residual water molecules trapped between MXene layers, which have a significant effect on electrical resistance of the MXene network. We observed larger changes in resistance and mass for MXenes exposed to air than MXenes exposed to water vapor, suggesting that interaction of MXene films with components of air has a significant effect on charge transport.

METHODS

Materials. Intercalated MXenes used in this study were synthesized similar to those reported by Ghidiu *et al.*[7] In short, Ti_3AlC_2 (the synthesis details of Ti_3AlC_2 can be found elsewhere[2]) was etched using a solution of LiCl dissolved in 10 wt% HF (1 g Ti_3AlC_2/10 mL of etching solution and Ti_3AlC_2/LiCl ~ 1:5 molar ratio) at room temperature for 24 h. After etching, the mixture was centrifuged, the top liquids were decanted, and fresh deionized water was added to the settled powder. The steps of adding fresh DI water, centrifuging, and decanting the liquids were repeated multiple times until pH of the decanted liquid was >5. Afterward, the settled powders were rinsed with 37% HCl (30 mL of 37% HCl: 1 g of powder) then centrifuged, and the liquids were decanted followed by adding fresh HCl. These HCl washing steps were repeated four times. After the HCl washing steps, fresh DI water was used to remove any traces of HCl. While the powders were still wet, they were divided into three portions. One of the portions was vacuum filtered to dry at room temperature (referred as pristine Ti_3C_2). For the other two, one of them was soaked in 1.0 M KCl in DI water and the other in 0.5 M $MgCl_2$ in DI water, both for 1 h (40 mL of solution: 1 g of powder). Afterward, the mixtures were centrifuged, and the liquids were decanted; the settled powders were soaked for 24 h in fresh solutions of their corresponding salts (1.0 M KCl for one sample and 0.5 M $MgCl_2$ for the other). Then the mixture was centrifuged, the liquids were decanted, and fresh DI water was added to remove any excess salts, followed by centrifugation and decanting of liquids. The water-washing step was repeated twice. The washed powders were filtered using a vacuum-assisted filtration setup and allowed to dry freely in air. All the treatments described above were conducted at room temperature.

QENS Measurements. QENS measurements were performed using high flux backscattering spectrometer (HFBS)[39] at NIST Center for Neutron Research. Neutrons of wavelength (λ) 6.271 Å with a corresponding energy of 2.080 meV were detected. The instrument has a Si(111) monochromator and 16 arrays of analyzer crystals that provide the energy resolution of 0.8 μeV (full width at half-maximum) covering 0.25 to 1.74 $Å^{-1}$ in Q (Q is momentum transfer vector, $Q = \frac{4\pi \sin\theta}{\lambda}$, 2θ is the scattering angle) and ±16 μeV in energy. Dry (vacuum-annealed at 110 °C) samples were placed into a flat aluminum plate sample holder of 0.25 mm thickness and were sealed with indium inside a dry Ar-filled glovebox. Each sample was cooled to 4 K, and QENS data were collected for instrument resolution. Fixed window scan was conducted on heating from 4 to 300 K at a rate of 2 K/min. Elastic intensity as a function of temperature for each sample was obtained after summing the intensity from all detectors. QENS data were grouped into eight groups. Data were reduced and analyzed using DAVE software.[40]

Neutron Total Scattering. Data were collected on the NOMAD beamline at the Spallation Neutron Source, Oak Ridge National Laboratory, as described by Neuefeind *et al.*[41] Two as-synthesized cation/H_2O-intercalated MXene powder samples (referred to as hydrated Mg-Ti_3C_2 and K-Ti_3C_2), two vacuum-dried samples (referred to as dry Mg-Ti_3C_2 and K-Ti_3C_2), and two D_2O rehydrated samples (referred to as rehydrated Mg-Ti_3C_2 and K-Ti_3C_2) were loaded into a 2

mm quartz capillary sealed with hot-melt adhesive. Dry samples are produced at 200 °C in a rough pumped vacuum oven for 14 h to ensure complete removal of intercalated H_2O molecules while leaving interlayer cations and surface terminations intact. To ensure reversibility of D_2O intercalation, the rehydrated samples were prepared by adding drops of D_2O water into the dry sample powers placed inside the N_2-filled glovebox and then loaded into the quartz capillary. Each sample was measured for ∼2 h at room temperature (∼22 °C). The observed raw intensities were first normalized by scattering from a vanadium rod (corrected for absorption and multiple scattering), and background scattering from the empty container and instrument was subtracted. The beamline's autoreduction software was used for data reduction, and the further normalization to the expected sample composition was performed *via* an iterative checking procedure in which the high-Q (40−50 Å^{-1}) and low-Q (0.3−1 Å^{-1}) backgrounds and their intensity ratios were compared with the calculated scattering ratio based on estimated stoichiometry and sample packing fraction. The high-Q *versus* low-Q ratio is used to determine the incoherent scattering fraction, which inherently reflects the amount of hydrogen (per formula units) contained in the studied material system. Their absolute values, on the contrary, reflect amounts of material exposed to neutrons, taking packing fraction into account. Therefore, proper normalization with respective sample composition and packing fraction results in the so-called total scattering structure function, $S(Q)$, the intensity of which oscillates around 1 in the limits of high-Q.

STEM. TEM samples of K^+- and Mg^{2+}-intercalated $Ti_3C_2T_x$ were prepared using Leica EM UC7 ultramicrotome after embedding MXene powder samples in epoxy. Epoxy slices containing the MXene powder were microtomed to around 50−75 nm and were then transferred to lacey carbon grids. A Nion UltraSTEM 100 microscope operated at 100 kV and equipped with a probe aberration corrector was used to acquire STEM images with spatial resolution at around 1 Å. STEM images were acquired using a high-angle annular dark-field with acceptance angle range from 86 to 200 mrad.

Sensing and TGA. Solutions of K- and Mg-intercalated MXenes (∼34% MXene by weight) were sonicated in DI water for 1 h. Using a precision pipet, 1 μL of each MXene solution was drop-cast on a precleaned 5 MHz AT-cut gold-coated quartz crystal microbalance and a SiO_2 substrate with prepatterned interdigitated gold electrodes spaced 2 μm apart. The MXene solutions cast on QCM and SiO_2 substrates formed films composed of networks of H_2O-intercalated flakes. Prior to H_2O vapor sorption measurements, films were placed under 10^{-3} Torr (1.33×10^{-3} mbar) vacuum for 12 h. The QCM crystals were driven by open-source Pierce oscillator circuits (OpenQCM).[42] Frequency shift was measured by Arduino micro microcontroller boards. Frequency shift of the QCM crystals was converted to mass change using the well-known Sauerbrey equation.[30] To increase resolution of the QCM signal, a 10 s gate time was implemented. Increasing the gate time enables sub-0.1 Hz frequency resolution during vacuum-based QCM measurements.[43] The 10 s gate time was sufficient to measure the slow kinetics of water sorption/desorption on MXenes. Electrical resistance was recorded using a Keithley 2420 sourcemeter. Water vapor pressure inside the vacuum chamber was regulated with a mass flow controller. A LabVIEW program was used to record data and control the QCM, Keithley 2420, and mass flow controller. During the experiment, samples were exposed to 90 min long pulses of H_2O vapor corresponding to P/P_0 = 0.05, 0.2, 0.4, and 0.8, where P/P_0 is the ratio of H_2O vapor pressure to H_2O vapor saturation pressure at 27 °C, so that P/P_0 corresponds to RH. All measurements were performed at 27 ± 0.5 °C inside a modified controlled environmental chamber from Surface Measurement Systems Ltd. Thermogravimetric analysis was carried out using a Discovery TGA from TA Instruments. TGA was performed on MXene powders under nitrogen flow after samples were exposed to air. During the experiment, temperature was ramped from room temperature to 400 °C at a rate of 20 °C/min.

Submerged QCM. We measured water intercalation in completely submerged MXenes using a a precleaned 5 MHz AT-cut gold-coated QCM (SRS QCM200) before and after flooding the cell with liquid. The frequency change between the bare crystal and the vacuum-dried (80 °C) MXene-coated crystal was used as a mass measurement of drop-casted MXenes. Absolute ethanol was used as a null result for the K- and Mg-intercalated MXene, as well as water interacting with the raw MXene, as the hydrodynamic and mass response of these would be similar because no intercalation was expected to take place. Secondary confirmation of water intercalation in submerged solutions was conducted through the addition of a single drop (0.1 mL) of water to the ethanol-filled QCM cells (3 mL), which resulted in similar mass increase as the pure water experiments. Measurements were taken every 3 h in a temperature-controlled environment.

Calculations. We used classical and DFT-based simulations to interpret the experimentally observed response of K^+- and Mg^{2+}-intercalated MXenes to hydration. Classical molecular dynamics were performed using LAMMPS software package.[44] Water molecules were represented by the SPC/E model;[45] Mg−H_2O interaction parameters were taken from literature,[46] and H_2O−MXene interaction parameters, summarized in Tables S1−S3, were optimized by matching DFT-based pair distribution functions between water and MXene surfaces.[47] Mg−MXene interactions were derived using the Lorentz−Berthelot combining rules, but since in this case Mg ions do not come in direct contact with the MXene surface, their actual influence is negligible. More details about the force field used are given in Supporting Information. Density functional calculations were performed using the plane-wave projector-augmented wave formalism[48,49] as implemented in the VASP[50−53] code. We utilized the PBE[54] density functional with Grimme D2 van der Waals corrections.[55] For dynamics calculations, a temperature of 295K was used in both types of simulation.

ASSOCIATED CONTENT

Ⓢ Supporting Information

The Supporting Information is available free of charge on the ACS Publications website at DOI: 10.1021/acsnano.7b05264.

Figures S1 and S2 and Tables S1−S4 as described in text (PDF)

AUTHOR INFORMATION

Corresponding Authors
*E-mail: naguibma@ornl.gov.
*E-mail: ivanovin@ornl.gov.

ORCID Ⓘ
Eric S. Muckley: 0000-0001-7114-5424
Michael Naguib: 0000-0002-4952-9023
Hsiu-Wen Wang: 0000-0002-2802-4122
Lukas Vlcek: 0000-0003-4782-7702
Naresh C. Osti: 0000-0002-0213-2299
Xiahan Sang: 0000-0002-2861-6814
Eugene Mamontov: 0000-0002-5684-2675
Katharine L. Page: 0000-0002-9071-3383
Jagjit Nanda: 0000-0002-6875-0057

Author Contributions
○E.S.M. and M.N. contributed equally.

Notes

REFERENCES

(1) Naguib, M.; Mochalin, V. N.; Barsoum, M. W.; Gogotsi, Y. 25th Anniversary Article: MXenes: A New Family of Two-Dimensional Materials. *Adv. Mater.* **2014**, *26*, 992−1005.

(2) Naguib, M.; Kurtoglu, M.; Presser, V.; Lu, J.; Niu, J.; Heon, M.; Hultman, L.; Gogotsi, Y.; Barsoum, M. W. Two-Dimensional Nanocrystals Produced by Exfoliation of Ti_3AlC_2. *Adv. Mater.* **2011**, *23*, 4248−4253.

(3) Naguib, M.; Mashtalir, O.; Carle, J.; Presser, V.; Lu, J.; Hultman, L.; Gogotsi, Y.; Barsoum, M. W. Two-Dimensional Transition Metal Carbides. *ACS Nano* **2012**, *6*, 1322−1331.

(4) Barsoum, M. W. *MAX Phases: Properties of Machinable Ternary Carbides and Nitrides*; John Wiley & Sons, 2013.

(5) Ying, Y.; Liu, Y.; Wang, X.; Mao, Y.; Cao, W.; Hu, P.; Peng, X. Two-Dimensional Titanium Carbide for Efficiently Reductive Removal of Highly Toxic Chromium (Vi) From Water. *ACS Appl. Mater. Interfaces* **2015**, *7*, 1795−1803.

(6) Ling, Z.; Ren, C. E.; Zhao, M.-Q.; Yang, J.; Giammarco, J. M.; Qiu, J.; Barsoum, M. W.; Gogotsi, Y. Flexible and Conductive MXene Films and Nanocomposites with High Capacitance. *Proc. Natl. Acad. Sci. U. S. A.* **2014**, *111*, 16676−16681.

(7) Ghidiu, M.; Halim, J.; Kota, S.; Bish, D.; Gogotsi, Y.; Barsoum, M. W. Ion-Exchange and Cation Solvation Reactions in Ti_3C_2 MXene. *Chem. Mater.* **2016**, *28*, 3507−3514.

(8) Ghidiu, M.; Lukatskaya, M. R.; Zhao, M.-Q.; Gogotsi, Y.; Barsoum, M. W. Conductive Two-Dimensional Titanium Carbide 'Clay' with High Volumetric Capacitance. *Nature* **2014**, *516*, 78−81.

(9) Lukatskaya, M. R.; Mashtalir, O.; Ren, C. E.; Dall'Agnese, Y.; Rozier, P.; Taberna, P. L.; Naguib, M.; Simon, P.; Barsoum, M. W.; Gogotsi, Y. Cation Intercalation and High Volumetric Capacitance of Two-dimensional Titanium Carbide. *Science* **2013**, *341*, 1502−1505.

(10) Xu, B.; Zhu, M.; Zhang, W.; Zhen, X.; Pei, Z.; Xue, Q.; Zhi, C.; Shi, P. Ultrathin MXene-Micropattern-Based Field-Effect Transistor for Probing Neural Activity. *Adv. Mater.* **2016**, *28*, 3333−3339.

(11) Mashtalir, O.; Naguib, M.; Mochalin, V. N.; Dall'Agnese, Y.; Heon, M.; Barsoum, M. W.; Gogotsi, Y. Intercalation and Delamination of Layered Carbides and Carbonitrides. *Nat. Commun.* **2013**, *4*, 1716.

(12) Karlsson, L. H.; Birch, J.; Halim, J.; Barsoum, M. W.; Persson, P. O. Atomically Resolved Structural and Chemical Investigation of Single MXene Sheets. *Nano Lett.* **2015**, *15*, 4955−4960.

(13) Hope, M. A.; Forse, A. C.; Griffith, K. J.; Lukatskaya, M. R.; Ghidiu, M.; Gogotsi, Y.; Grey, C. P. NMR Reveals the Surface Functionalisation of Ti_3C_2 MXene. *Phys. Chem. Chem. Phys.* **2016**, *18*, 5099−5102.

(14) Osti, N. C.; Naguib, M.; Ostadhossein, A.; Xie, Y.; Kent, P. R. C.; Dyatkin, B.; Rother, G.; Heller, W. T.; van Duin, A. C. T.; Gogotsi, Y.; Mamontov, E. Effect of Metal Ion Intercalation on the Structure of MXene and Water Dynamics on its Internal Surfaces. *ACS Appl. Mater. Interfaces* **2016**, *8*, 8859−8863.

(15) Gan, L.-Y.; Huang, D.; Schwingenschlögl, U. Oxygen Adsorption and Dissociation During the Oxidation of Monolayer Ti_2C. *J. Mater. Chem. A* **2013**, *1*, 13672−13678.

(16) Merrill, P. B.; Perry, S. S.; Frantz, P.; Didziulis, S. V. Adsorption of water on TiC (100): Evidence for Complex Reaction and Desorption Pathways. *J. Phys. Chem. B* **1998**, *102*, 7606−7612.

(17) Didziulis, S. V.; Frantz, P.; Perry, S. S.; El-bjeirami, O.; Imaduddin, S.; Merrill, P. B. Substrate-Dependent Reactivity of Water on Metal Carbide Surfaces. *J. Phys. Chem. B* **1999**, *103*, 11129−11140.

(18) Wang, H.-W.; Naguib, M.; Page, K.; Wesolowski, D. J.; Gogotsi, Y. Resolving the Structure of Ti3C2Tx MXenes through Multilevel Structural Modeling of the Atomic Pair Distribution Function. *Chem. Mater.* **2016**, *28*, 349−359.

(19) Hope, M. A.; Forse, A. C.; Griffith, K. J.; Lukatskaya, M. R.; Ghidiu, M.; Gogotsi, Y.; Grey, C. P. NMR Reveals the Surface Functionalisation of Ti_3C_2 MXene. *Phys. Chem. Chem. Phys.* **2016**, *18*, 5099−5102.

(20) Naguib, M.; Halim, J.; Lu, J.; Cook, K. M.; Hultman, L.; Gogotsi, Y.; Barsoum, M. W. New Two-Dimensional Niobium and Vanadium Carbides as Promising Materials for Li-ion Batteries. *J. Am. Chem. Soc.* **2013**, *135*, 15966−15969.

(21) Ghidiu, M.; Naguib, M.; Shi, C.; Mashtalir, O.; Pan, L. M.; Zhang, B.; Yang, J.; Gogotsi, Y.; Billinge, S. J. L.; Barsoum, M. W. Synthesis and Characterization of Two-Dimensional Nb_4C_3 (MXene). *Chem. Commun.* **2014**, *50*, 9517−9520.

(22) Khazaei, M.; Ranjbar, A.; Arai, M.; Sasaki, T.; Yunoki, S. Electronic Properties and Applications of MXenes: a Theoretical Review. *J. Mater. Chem. C* **2017**, *5*, 2488−2503.

(23) Shannon, R. Revised Effective Ionic Radii and Systematic Studies of Interatomic Distances in Halides and Chalcogenides. *Acta Crystallogr., Sect. A: Cryst. Phys., Diffr., Theor. Gen. Crystallogr.* **1976**, *32*, 751−767.

(24) Nightingale, E. R. Phenomenological Theory of Ion Solvation. Effective Radii of Hydrated Ions. *J. Phys. Chem.* **1959**, *63*, 1381−1387.

(25) Singwi, K.; Sjölander, A. Diffusive Motions in Water and Cold Neutron Scattering. *Phys. Rev.* **1960**, *119*, 863−871.

(26) Teixeira, J.; Bellissentfunel, M. C.; Chen, S. H.; Dianoux, A. J. Experimental-Determination of the Nature of Diffusive Motions of Water-Molecules at Low-Temperatures. *Phys. Rev. A: At., Mol., Opt. Phys.* **1985**, *31*, 1913−1917.

(27) Osti, N. C.; Cote, A.; Mamontov, E.; Ramirez-Cuesta, A.; Wesolowski, D. J.; Diallo, S. O. Characteristic Features of Water Dynamics in Restricted Geometries Investigated with Quasi-Elastic Neutron Scattering. *Chem. Phys.* **2016**, *465*, 1−8.

(28) Malikova, N.; Cadène, A.; Marry, V.; Dubois, E.; Turq, P. Diffusion of Water in Clays on the Microscopic Scale: Modeling and Experiment. *J. Phys. Chem. B* **2006**, *110*, 3206−3214.

(29) Michot, L. J.; Delville, A.; Humbert, B.; Plazanet, M.; Levitz, P. Diffusion of Water in a Synthetic Clay with Tetrahedral Charges by Combined Neutron Time-of-Flight Measurements and Molecular Dynamics Simulations. *J. Phys. Chem. C* **2007**, *111*, 9818−9831.

(30) Sauerbrey, G. Verwendung von Schwingquarzen zur Wägung dünner Schichten und zur Mikrowägung. *Eur. Phys. J. A* **1959**, *155*, 206−222.

(31) Shpigel, N.; Levi, M. D.; Sigalov, S.; Girshevitz, O.; Aurbach, D.; Daikhin, L.; Pikma, P.; Marandi, M.; Janes, A.; Lust, E.; Jackel, N.; Presser, V. *In situ* Hydrodynamic Spectroscopy for Structure Character-

ization of Porous Energy Storage Electrodes. *Nat. Mater.* **2016**, *15*, 570−575.

(32) Shpigel, N.; Lukatskaya, M. R.; Sigalov, S.; Ren, C. E.; Nayak, P.; Levi, M. D.; Daikhin, L.; Aurbach, D.; Gogotsi, Y. In Situ Monitoring of Gravimetric and Viscoelastic Changes in 2D Intercalation Electrodes. *ACS Energy Lett.* **2017**, *2*, 1407−1415.

(33) Krutovertsev, S.; Tarasova, A.; Krutovertseva, L.; Zorin, A. Integrated Multifunctional Humidity Sensor. *Sens. Actuators, A* **1997**, *62*, 582−585.

(34) Bi, H.; Yin, K.; Xie, X.; Ji, J.; Wan, S.; Sun, L.; Terrones, M.; Dresselhaus, M. S. Ultrahigh Humidity Sensitivity of Graphene Oxide. *Sci. Rep.* **2013**, *3*, 2714.

(35) Li, Y.; Yang, M. Humidity Sensitive Properties of a Novel Soluble Conjugated Copolymer: Ethynylbenzene-co-Propargyl Alcohol. *Sens. Actuators, B* **2002**, *85*, 73−78.

(36) Chen, Z.; Lu, C. Humidity Sensors: a Review of Materials and Mechanisms. *Sens. Lett.* **2005**, *3*, 274−295.

(37) Lipatov, A.; Alhabeb, M.; Lukatskaya, M. R.; Boson, A.; Gogotsi, Y.; Sinitskii, A. Effect of Synthesis on Quality, Electronic Properties and Environmental Stability of Individual Monolayer Ti_3C_2 MXene Flakes. *Adv. Electron. Mater.* **2016**, *2*, 1600255.

(38) Levi, M. D.; Lukatskaya, M. R.; Sigalov, S.; Beidaghi, M.; Shpigel, N.; Daikhin, L.; Aurbach, D.; Barsoum, M. W.; Gogotsi, Y. Solving the Capacitive Paradox of 2D MXene using Electrochemical Quartz-Crystal Admittance and In Situ Electronic Conductance Measurements. *Adv. Energy Mater.* **2015**, *5*, 1400815.

(39) Meyer, A.; Dimeo, R.; Gehring, P.; Neumann, D. The High-Flux Backscattering Spectrometer at the NIST Center for Neutron Research. *Rev. Sci. Instrum.* **2003**, *74*, 2759−2777.

(40) Azuah, R. T.; Kneller, L. R.; Qiu, Y. M.; Tregenna-Piggott, P. L. W.; Brown, C. M.; Copley, J. R. D.; Dimeo, R. M. DAVE: A Comprehensive Software Suite for the Reduction, Visualization, and Analysis of Low Energy Neutron Spectroscopic Data. *J. Res. Natl. Inst. Stand. Technol.* **2009**, *114*, 341−358.

(41) Neuefeind, J.; Feygenson, M.; Carruth, J.; Hoffmann, R.; Chipley, K. K. The Nanoscale Ordered Materials Diffractometer NOMAD at the Spallation Neutron Source SNS. *Nucl. Instrum. Methods Phys. Res., Sect. B* **2012**, *287*, 68−75.

(42) Muckley, E. S.; Anazagasty, C.; Jacobs, C. B.; Hianik, T.; Ivanov, I. N. *Low-Cost Scalable Quartz Crystal Microbalance Array for Environmental Sensing*, SPIE Organic Photonics + Electronics; International Society for Optics and Photonics, 2016; pp99440Y.

(43) Bieri, M.; Bürgi, T. Adsorption Kinetics of L-Glutathione on Gold and Structural Changes During Self-Assembly: an *In Situ* ATR-IR and QCM study. *Phys. Chem. Chem. Phys.* **2006**, *8*, 513−520.

(44) Plimpton, S. Fast Parallel Algorithms for Short-Range Molecular Dynamics. *J. Comput. Phys.* **1995**, *117*, 1−19.

(45) Berendsen, H. J. C.; Grigera, J. R.; Straatsma, T. P. The Missing Term In Effective Pair Potentials. *J. Phys. Chem.* **1987**, *91*, 6269−6271.

(46) Mamatkulov, S.; Fyta, M.; Netz, R. R. Force Fields for Divalent Cations Based on Single-Ion and Ion-Pair Properties. *J. Chem. Phys.* **2013**, *138*, 024505.

(47) Vlcek, L.; Chialvo, A. A. Rigorous Force Field Optimization Principles Based on Statistical Distance Minimization. *J. Chem. Phys.* **2015**, *143*, 144110.

(48) Blöchl, P. E. Projector Augmented-Wave Method. *Phys. Rev. B: Condens. Matter Mater. Phys.* **1994**, *50*, 17953−17979.

(49) Kresse, G.; Joubert, D. From Ultrasoft Pseudopotentials to the Projector Augmented-Wave method. *Phys. Rev. B: Condens. Matter Mater. Phys.* **1999**, *59*, 1758−1775.

(50) Kresse, G.; Hafner, J. *Ab initio* Molecular Dynamics for Liquid Metals. *Phys. Rev. B: Condens. Matter Mater. Phys.* **1993**, *47*, 558−561.

(51) Kresse, G.; Hafner, J. *Ab initio* Molecular-Dynamics Simulation of the Liquid-Metal−Amorphous-Semiconductor Transition in Germanium. *Phys. Rev. B: Condens. Matter Mater. Phys.* **1994**, *49*, 14251−14269.

(52) Kresse, G.; Furthmüller, J. Efficient Iterative Schemes for Ab initio Total-Energy Calculations Using a Plane-Wave Basis Set. *Phys. Rev. B: Condens. Matter Mater. Phys.* **1996**, *54*, 11169−11186.

(53) Kresse, G.; Furthmüller, J. Efficiency of Ab-Initio Total Energy Calculations for Metals and Semiconductors Using a Plane-Wave Basis Set. *Comput. Mater. Sci.* **1996**, *6*, 15−50.

(54) Perdew, J. P.; Burke, K.; Ernzerhof, M. Generalized Gradient Approximation Made Simple. *Phys. Rev. Lett.* **1996**, *77*, 3865−3868.

(55) Grimme, S. Semiempirical GGA-Type Density Functional Constructed with a Long-Range Dispersion Correction. *J. Comput. Chem.* **2006**, *27*, 1787−1799.